Article

Robust Oxygen Evolution on Ni-Doped MoO₃: Overcoming Activity–Stability Trade-Off in Alkaline Water Splitting

Published as part of Chem & Bio Engineering special issue "Electrochemical Engineering for Sustainability".

Ankit Kumar Verma, Shahan Atif, Abhisek Padhy, Tej S. Choksi, Prabeer Barpanda, and Ananth Govind Rajan*

Cite This: *Chem Bio Eng.* 2025, 2, 241–252
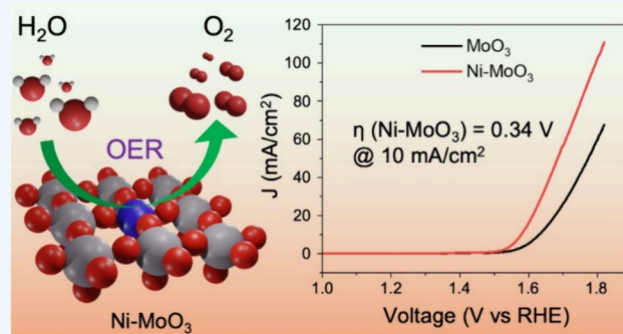
Read Online

ACCESS | 📊 Metrics & More | 📖 Article Recommendations | SI Supporting Information

ABSTRACT: Electrochemical water splitting using earth-abundant materials is crucial for enabling green hydrogen production and energy storage. In recent years, molybdenum trioxide (MoO_3), a semiconducting material, has been proposed as a candidate catalyst for the oxygen evolution reaction (OER). Here, we advance nickel (Ni) doping of MoO_3 as a strategy to increase the activity and stability of the material during alkaline electrochemical water splitting, thereby overcoming the typical activity-stability trade-off encountered with OER catalysts. The instability of MoO_3 in alkaline media can be mitigated by doping with Ni, whose oxide is stable under such conditions. Using density functional theory (DFT) with Hubbard corrections, we show that Ni doping reduces the thermodynamic OER overpotential on the MoO_3 basal plane to 0.64 V. Experiments demonstrate that Ni-doped MoO_3 requires an overpotential of 0.34 V for an OER current density of 10 mA/cm² (and 0.56 V at 100 mA/cm²), as opposed to a value of 0.40 V for pure MoO_3. Further, Ni-doped MoO_3 exhibits a lower Tafel slope of 74.8 mV/dec, compared to 98.3 mV/dec for the pristine material under alkaline conditions. While Mo leaches in alkaline conditions, X-ray photoelectron spectroscopy reveals enhanced stability with Ni doping. Overall, our work advances Ni-doped MoO_3 as a promising water-splitting electrocatalyst and provides new insights into its OER mechanism and stability in alkaline media. More generally, the work sheds light on choosing a dopant to increase a material's activity and stability, which will also find applications in other catalytic materials.

KEYWORDS: *MoO₃, DFT + U, Doping, Oxygen Evolution Reaction, Water Splitting*

■ INTRODUCTION

Hydrogen (H_2), an important industrial gas, has also emerged as a promising alternative to fossil fuels. Its application areas include energy production in fuel cells and several industries, such as fertilizer manufacturing, metal processing, and biomass/petroleum hydrotreating.[1,2] Conventionally, H_2 is produced using steam methane reforming, a process that releases a considerable amount of carbon dioxide (CO_2) into the atmosphere. Concerns about global warming have necessitated the discovery of alternative synthesis routes to produce green (i.e., CO_2-emission-free) H_2, the most promising of which are thermochemical[3] and (photo)-electrochemical[4,5] water splitting. Electrocatalytic H_2 production offers an efficient route to enable the conversion of renewable electricity into H_2, thereby facilitating effective energy storage and conversion.[6,7] The cathodic hydrogen evolution reaction (HER) and the anodic oxygen evolution reaction (OER) are the fundamental half-cell reactions involved in water splitting. Notably, the OER is kinetically sluggish due to the presence of four proton-coupled electron transfer steps,[4,8] and the high energy requirement for making oxygen–oxygen bonds (O═O), which hinder both the advancement and scalability of water-splitting technology.[9] Under alkaline conditions, wherein hydroxide ions are involved, the OER can be written as $4OH^- \rightarrow O_2 + 2H_2O + 4e^-$. Overall, this reaction requires 4.92 eV of energy per O_2 molecule produced at room temperature and 1 bar pressure, representing a significant energy input.[10] Therefore, developing and exploring stable, economically viable, and highly efficient catalysts for the OER beyond the conventional iridium and

ACS Publications

ruthenium-based oxide catalysts is of utmost significance in generating environmentally friendly H_2.

Inexpensive transition metal-based oxide materials have become the focus of intense research attention due to their proven effectiveness in gas/analyte sensing, energy conversion/ storage devices, and electro/photocatalysis.[11−13] In recent decades, there has been significant exploration into transition metal-based OER electrocatalysts, including nickel and iron oxides and (oxy)hydroxides,[14,15] driven by the goal of reducing dependency on expensive and limited noble metal-based catalysts. Although noble metal oxides like IrO_2 and RuO_2 are currently the most active OER catalysts in acidic conditions, they are hindered by material scarcity and a loss of activity over extended use.[16,17] Conversely, while affordable transition-metal hydroxides and oxyhydroxides (Ni, Co, Fe) are effective OER catalysts in alkaline electrolytes,[18,19] they face significant challenges due to high overpotentials and a trade-off between activity and stability, which limits their practical application, similar to other catalysts.[20,21] An optimal catalyst should offer a balanced dissolution rate that is neither too fast nor too slow so it is both stable and active.

Molybdenum trioxide (MoO_3) is garnering attention for its versatile structural and functional properties among transition metal oxides. Its ability to modify oxidation states through electron acceptance in d orbitals contributes to its adaptability, making it promising for diverse technological applications.[22,23] In this regard, modulating the electronic structure is crucial in improving the catalytic activity and stability of a catalyst. It can be achieved by elemental doping,[24−26] defect engineering,[27,28] and deposition on a suitable host material.[29] Tuning the electronic configuration of the catalyst by doping can significantly influence the binding energy of the intermediate species involved in the OER mechanism. Stability and activity are crucial required properties of any catalyst,[30] and it has been shown that dopants can dramatically reduce the OER overpotential on many catalyst materials.[25,31] Nickel is a nonprecious metal and has been reported as a promising dopant due to its efficient catalytic activity.[24,32−34] Ni dopant atoms can alter the doped catalyst's oxidation state, electronic structure, and surface area, improving catalytic activity. For instance, doping Ni at an octahedral site in the surface layer of Co_3O_4 reduced the simulated thermodynamic OER overpotential from 0.46 V to 0.34 V.[34] In another study, Ni doping significantly enhanced the measured OER activity of a Bi_2WO_6 electrode, demonstrating a comparatively low overpotential of 0.242 V along with high stability.[32] Additionally, 3% Ni-doped CuS nanocrystals demonstrate significantly improved OER activity, with an overpotential of 0.39 V to achieve a current density of 10 mA cm^{-2} and a Tafel slope of 96.8 mV/dec, outperforming undoped CuS.[33] Overall, Ni doping has emerged as an effective strategy to enhance the water-splitting activity of various materials. Accordingly, this work examines the OER activity and stability of pure and Ni-doped MoO_3, employing quantum-mechanical density functional theory (DFT) calculations alongside experiments to develop efficient and inexpensive Ni-MoO_3-based OER electrocatalysts.

Previously, molybdenum sulfide, carbide, and their derivatives have been employed as HER catalysts.[35−37] However, their utilization as OER electrocatalysts remains infrequent, with limited reported instances in the literature. Several previous studies focused on using noble metals to improve the OER activity of MoO_3. For example, Ag doping in MoO_3 significantly enhanced its OER activity under alkaline conditions.[38] Additionally, an IrO_2/MoO_3 hybrid reduced the overpotential by 0.11 V compared to the benchmark catalyst IrO_2, leading to similar required overpotentials of 0.34 V and 0.36 V, respectively, under acidic and alkaline conditions, at a current density of 10 mA cm^{-2}.[39] Researchers have also explored doping MoO_3 with non-noble metal dopants. For example, Li et al. synthesized a bifunctional MoO_3/Ni-NiO composite nanomaterial using a sequential electrodeposition technique. This composite, again under alkaline solution conditions, demonstrated outstanding electrocatalytic properties, with a low overpotential of 0.062 V at 10 mA/cm^2.[40] The very low overpotential in this study is likely due to the deposition of ultrafine MoO_3 and Ni nanoparticles on amorphous NiO nanosheets, which could have led to a larger electrochemically active surface area. However, using ultrafine nanoparticles led to the sample being investigated to show 2.1% chronopotentiometric deterioration over 20 h of catalyst testing. In another study, Kim et al. enhanced the OER activity of MoO_3 by incorporating Li ions into its structure through the lithiation of MoO_3 nanoparticles deposited on carbon fiber paper, resulting in an overpotential of 0.46 V at 10 mA/cm^2 in aqueous KOH.[41] Another recent theoretical study explored the use of alkali metals in enhancing the OER activity of transition-metal doped monolayer MoO_3.[42] Moreover, MoO_3 patches have also demonstrated effectiveness in enhancing the catalytic activity of Ni oxyhydroxide nanosheets, exhibiting an overpotential of 0.26 V at 10 mA/cm^2 in aqueous NaOH.[43] Additionally, Kundu et al. created oxygen vacancies in $NiMoO_4$ nanorods within a two-electrode system, showing a current density of 10 mA/cm^2 with an overpotential of 0.36 V in 1 M KOH.[44] Despite this progress, previous experimental work has not explored inexpensive transition-metal doping, for example, using nickel, to enhance the OER activity of MoO_3. Moreover, a key aspect that has received insufficient attention is the stability of MoO_3 under alkaline conditions, wherein most experimental studies, as seen above, have investigated its OER activity. Note that MoO_3 is an acidic oxide known to dissolve in alkaline solutions,[45] but no study on electrochemical water splitting has examined this point. In this regard, it is well-known that materials that transform under reaction conditions to a derivative form could lead to higher activity.[46] Nevertheless, this possibility has not been probed for either pure or doped MoO_3.

To address these knowledge gaps, in our work, we thoroughly investigate the OER activity of pure and Ni-doped MoO_3 using DFT and experiments to understand the OER mechanism on the MoO_3 basal plane and the stability of the material under alkaline solution conditions. The rationale for using Ni is that, since the oxides of Ni are stable under alkaline conditions, while MoO_3 is not, doping with the former element could improve not only the stability, but also the activity of MoO_3 by offering a balanced dissolution rate of the material. We employ Hubbard corrections in DFT (DFT + U) to accurately model the localized nature of the $3d$ and $4d$ electrons, respectively, in the Ni and Mo ions in the material. This approach corrects the self-interaction error prevalent in conventional DFT and allows a reasonable description of redox free energy changes. Our theoretical results reveal that Ni doping of MoO_3 is favorable, demonstrating a reduction in the thermodynamic OER overpotential by 0.49 V compared to bare MoO_3. Our experimental results, in qualitative agreement with the theoretical predictions, support the doping of MoO_3 by nickel to obtain promising OER activity. We synthesize the

catalyst using a solid-state route and characterize it via X-ray diffraction (XRD), X-ray photoelectron spectroscopy (XPS), and scanning electron microscopy (SEM). Linear sweep voltammetry is used to determine the current density−applied potential relationship, and chronopotentiometry is employed to study the stability of the developed catalyst. We determine the overpotential required for an OER current density of 10 mA cm^{-2} to be 0.34 V. We also show that Mo does indeed leach under the alkaline conditions of the OER, an aspect that has been ignored in the literature. Nevertheless, we demonstrate that Ni doping of the material reduces the extent of Mo leaching. Overall, we provide detailed insights into the OER reaction mechanism on both pure and Ni-doped MoO$_3$ and advance Ni doping as a promising strategy to enhance the OER activity and stability of MoO$_3$ under alkaline solution conditions.

■ METHODS

Details of the DFT Calculations. The electronic energy of all the intermediates was calculated via spin-polarized DFT + U calculations using the Vienna *Ab initio* Simulation Package (VASP), which employs plane wave basis sets.[47,48] The projector augmented wave (PAW) formalism was employed to model the ion-electron interactions[49,50] with a kinetic energy cutoff (E_{cut}) of 450 eV. The Perdew−Burke−Ernzerhof (PBE) exchange-correlation functional[51] with Hubbard corrections via the rotationally invariant approach proposed by Dudarev et al.[52] was employed, with the U-J values of 6.3 eV (ref 53) and 5.5 eV (ref 54) for the Mo and Ni atom centers, respectively. The DFT method, combined with the rotationally invariant on-site repulsion model, depends on a single parameter, U-J. To determine this value for Mo, Coquet and Willock used the atomic spin density from a cluster model as reference data. By optimizing the model and varying the U-J value, they observed a strong linear correlation between the spin population and U-J. The selected U-J value for Mo ensured the best agreement between the results of cluster and periodic models.[53] For Ni, Li and Selloni determined the U-J value using linear response theory, which analyzes the system's response to perturbations in electronic occupations. This approach ensures an accurate representation of Ni's electronic structure by optimizing the U-J parameter, accounting for electron−electron interactions, and minimizing the influence of periodic images.[54] For the bulk MoO$_3$ structure, the Brillouin zone was sampled by the Monkhorst−Pack k-point grid method,[55] and a 5 × 3 × 5 k-point mesh was decided after testing various grid meshes. The k-point mesh and E_{cut} were selected based on a 1.0 meV/atom convergence criterion for the system's ground-state energy. We considered a 3 × 3 supercell with four MoO$_3$ layers for the catalyst surface. Furthermore, a vacuum of 20 Å was used perpendicular to the surface to exclude the interaction between periodic images, and for this model, a 3 × 1 × 3 k-point mesh was used. The self-consistent energy convergence criterion was chosen to be 10^{-5} eV, and the structure was allowed to relax to a force threshold of 0.01 eV/Å. Moreover, dipole corrections to the DFT energy and DFT forces were also enforced in the direction perpendicular to the surface using the IDIPOL = 3 and LDIPOL = .TRUE. tags, respectively, in the VASP input file. In the case of molecules, i.e., water and hydrogen, dipole corrections were applied in all three directions by employing IDIPOL = 4 in place of IDIPOL = 3. We used Gaussian smearing with a width of 0.01 eV to improve DFT convergence by distributing the occupation of states around the Fermi level.

Details of the Free-Energy Calculations. The computational hydrogen electrode (CHE) framework, developed by Nørskov et al., was employed to determine the thermodynamics of the elementary reactions using a proton-coupled electron transfer (PCET) path-way.[56,57] The CHE framework provides a straightforward route to relate the electrochemical potential of electron−proton pairs to the Gibbs free energy of hydrogen molecules. Under standard conditions (pH = 0, T = 298.15 K, p = 1 bar), the standard Gibbs free energy of a

single electron−proton pair is taken to be half of the standard Gibbs free energy of a hydrogen molecule in the gas phase. While the free energies of electrochemical elementary steps scale linearly with the applied potential, nonelectrochemical elementary steps are considered unaffected by the applied potential. The standard Gibbs free energy of gaseous molecule i ($G_{i(g)}^0$) was calculated as follows

$$G_{i(g)}^0 = E_{i(g)}^{DFT} + ZPE_{i(g)}^{DFT}$$
$$+ \left(H^\circ(298.15K) - H^\circ(0K) - TS^\circ(298.15K)\right)_i^{exp} \quad (1)$$

where $E_{i(g)}^{DFT}$ represents the DFT energy of isolated molecule i in vacuum, $ZPE_{i(g)}^{DFT}$ is the zero-point energy of the isolated molecule, $H^0(T)$ is the experimental standard enthalpy at temperature T K, and $S^0(T)$ is the experimental standard entropy at temperature T K. The DFT and zero-point energy calculations were conducted using the PBE + U theoretical framework, and experimental standard enthalpy and entropy were obtained from the NIST-JANAF thermochemical tables.[58] We included an additional term to determine the Gibbs free energy of a water molecule in the liquid phase. This term, $\Delta G_{g \to l}^0(298.15 \text{ K})$, represents the Gibbs free energy of condensation of water molecules (−8.6 kJ/mol, sourced from the NIST-JANAF thermochemical tables[58]) at room temperature and is added into the above formula. After calculating the Gibbs free energy of the gaseous hydrogen ($G_{H_2(g)}^0$) and liquid water molecules ($G_{H_2O(l)}^0$), the Gibbs free energy of the gaseous oxygen molecule ($G_{O_2(g)}^0$) was determined by ensuring that the free energy change during the OER is 4.92 eV at 298.15 K:

$$G_{O_2(g)}^0 = 2G_{H_2O(l)}^0 - 2G_{H_2(g)}^0 + 4.92 \text{ eV} \quad (2)$$

The vibrational zero-point energies (ZPEs) for the gaseous species were calculated by summing up the contributions of N normal modes using the expression $\sum_j^N \left[\frac{1}{2}h\nu_j\right]$ where h denotes Planck's constant and ν_j represents the vibrational frequency of each normal mode. These normal modes were determined by DFT-PBE + U. Note that, in the case of the hydrogen molecule, there is one normal mode (N = 1), and for the water molecule, there are three normal modes (N = 3). The Gibbs free energy of the various adsorbed species (G_i^0) involved in the OER was calculated as follows
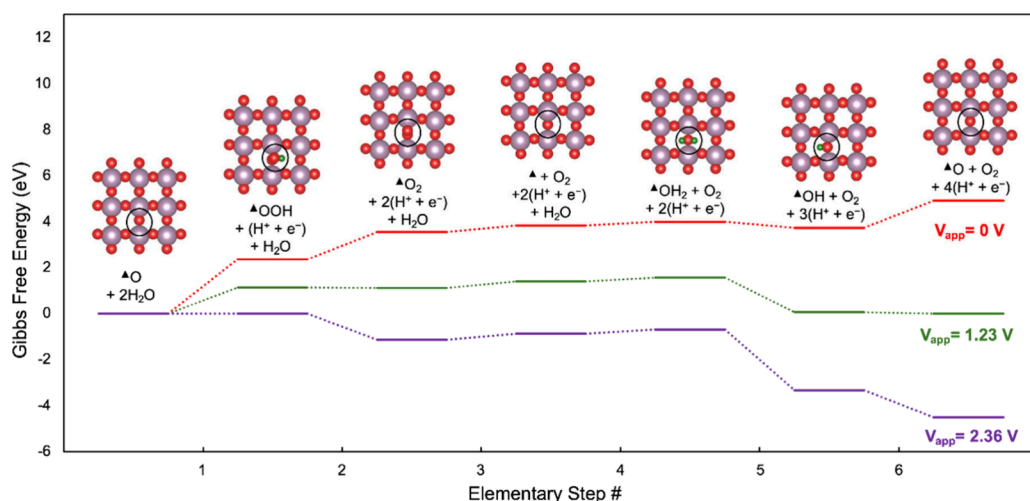
$$G_i^0 = E_i^{DFT} + E_{vib,i} - TS_{vib,i} \quad (3)$$

where E_i^{DFT} is the DFT + U-calculated potential energy of the MoO$_3$ lattice (bare/doped) with the intermediate species, $E_{vib,i}$ and $S_{vib,i}$ are the vibrational internal energy and vibrational entropy of the MoO$_3$ lattice (bare/doped) with intermediate species, respectively, and T is the temperature in kelvin. Note that the pressure−volume energy term is not considered for adsorbed intermediates due to its negligible effect in the solid phase. The following expressions were used to calculate the vibrational internal energy and vibrational entropy

$$E_{vib,i} = \sum_j^{3N_i} \left[\frac{1}{2}h\nu_{ji} + \frac{h\nu_{ji}}{e^{\beta h\nu_{ji}} - 1}\right] \quad (4)$$

$$TS_{vib,i} = \sum_j^{3N_i} \left[\frac{h\nu_{ji}}{e^{\beta h\nu_{ji}} - 1} - \frac{1}{\beta} \ln\left(1 - e^{-\beta h\nu_{ji}}\right)\right] \quad (5)$$

where ν_{ji} are the $3N_i$ normal modes for the N_i surface atoms in the intermediate, h is Planck's constant, and $\beta = \frac{1}{k_B T}$ (where k_B is the Boltzmann constant). The normal modes were calculated for all the absorbed species on the surface as well as for H$_2$ and H$_2$O molecules by using central differences where the atoms were displaced from their respective relaxed positions in all positive and negative directions (using the NFREE = 2 tag) with a displacement of 0.005 Å. We employed the programs developed by Henkelman et al. to enable the dynamical matrix calculation in VASP to obtain the normal-mode frequencies.[59]

Figure 1. Standard Gibbs free energy profile for the OER on the Mo-terminated (010) facet in pristine MoO_3. Inset figures depict top views of the relaxed structures. In these structures, molybdenum atoms are shown in lilac, oxygen in red, and hydrogen in green. The black outline denotes the active site in each intermediate. Results are shown for three different applied potentials (0 V in red; 1.23 V, the thermodynamic OER potential, in green; and 2.36 V, the determined thermodynamic onset potential, in purple).

Experimental Procedures. *Reagents.* Ammonium molybdate tetrahydrate $((NH_4)_6Mo_7O_{24}\cdot 4H_2O$, SD Fine Chem., 99%), nickel nitrate hexahydrate $(Ni(NO_3)_2\cdot 6H_2O$, SD Fine Chem., 99%), Super P carbon black (Sigma-Aldrich), Nafion (5 wt %, Sigma-Aldrich), and RuO_2 (Sigma-Aldrich, 99.9%) were procured from the listed suppliers with the stated purity. Merck Milli-Q water was used throughout the experiments.

Catalyst Preparation. The synthesis of pure and Ni-doped MoO_3 was carried out via a solid-state route. For Ni-doped MoO_3, ammonium molybdate tetrahydrate was thoroughly mixed with a 10% molar ratio of nickel nitrate hexahydrate using a mortar and pestle. The resultant mixture was then pelletized and annealed in air at 450 °C for 12 h (heating rate = 10 °C min^{-1}) in a muffle furnace. For pure MoO_3, nickel nitrate hexahydrate was excluded from the synthesis.

Catalyst Characterization. The phase and structural features of the synthesized catalysts were observed by analyzing X-ray diffraction (XRD) patterns on an X-ray diffractometer (PANalytical X'Pert Pro, Cu Kα, λ = 1.5406 Å, 40 kV, 40 mA). Surface morphologies were inspected using field emission scanning electron microscopy (FESEM) (Ultra55, Carl Zeiss AG) equipped with an EDS detector and a thermal field emission source (W) operating at 0.1–30 kV. The presence of various chemical elements and their oxidation states were determined by an X-ray photoelectron spectroscopy (XPS) AXIS ULTRA DLD (Kratos) spectrometer employing a monochromatic Al Kα 1486.6 eV excitation source. The Brunauer–Emmett–Teller (BET) surface areas of MoO_3 and Ni-doped MoO_3 were measured using a Quantachrome Autosorb iQ2 analyzer.

Electrochemical Measurements. The catalytic activity of pure and Ni-doped MoO_3 toward the OER was investigated using a CH Instruments, Inc. electrochemical workstation (760E, USA). All the electrochemical analyses were conducted at room temperature with a three-electrode configuration. Before the electrochemical studies, the catalyst was ground thoroughly with Super P (a conductive agent) in a weight ratio of 3:1. One mg of this mixture was then well dispersed in 95 μL of ethanol and 5 μL of Nafion. After sonication to achieve a uniform dispersion, 5 μL of this ink was coated onto a rotating ring disk electrode (RRDE; used as a working electrode), with a Pt wire as a counter electrode; for RuO_2, a glassy carbon electrode was used as the working electrode. For the chronopotentiometry and chronoamperometry stability tests, instead of an RRDE, a graphite sheet electrode was used with 100 μL of the ink coated onto it. Depending upon the electrolyte used, reference electrodes include Hg/HgO for alkaline and Ag/AgCl (in 3.5 M KCl) for acidic media. The electrochemical measurements were performed in freshly prepared 1

M KOH or 0.5 M H_2SO_4 electrolyte at room temperature. Polarization curves (linear sweep voltammetry) were recorded at a scan rate of 10 mV/s, and chronopotentiometry curves were recorded at a constant potential without *iR*-compensation. All potentials were reported relative to the reversible hydrogen electrode (RHE):

$$E_{RHE} = E^0_{Hg/HgO} + 0.059pH + E_{Hg/HgO} \quad (6)$$

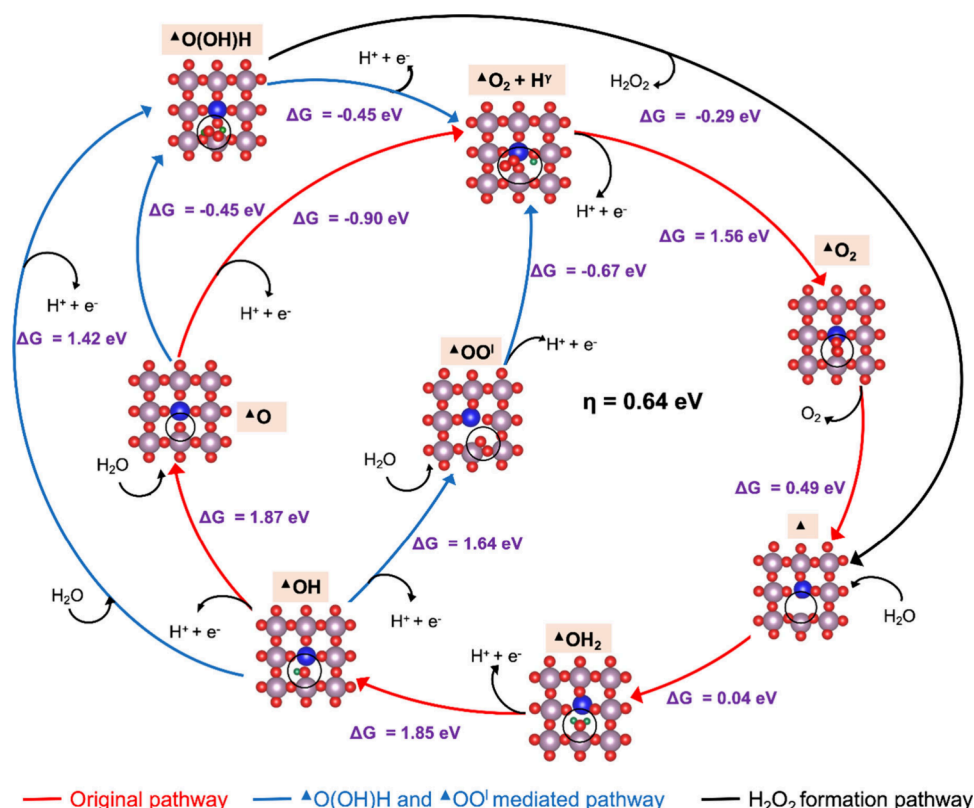$$E_{RHE} = E^0_{Ag/AgCl} + 0.059pH + E_{Ag/AgCl} \quad (7)$$

■ RESULTS AND DISCUSSION

Investigation of the OER Activity on the Mo-Terminated (010) Facet of Bare and Ni-Doped MoO_3 Using DFT + U. We considered orthorhombic MoO_3 because it is the most stable structure of the material.[60,61] Table S1 in the Supporting Information shows that the calculated lattice parameters matched reasonably well with experimentally determined ones.[62] Details regarding the computational parameters used are provided in the Methods section (see also Tables S2–S4). We analyzed the OER activity of the asymmetric oxygen active site of α-MoO_3 at the *Mo-terminated (010) facet*. This particular facet forms the basal plane of MoO_3 and has been investigated for its catalytic properties in previous studies.[63] We also considered the *O-terminated (010) facet* (Figure S1), but it exhibited 0.35 and 0.56 V higher overpotentials for bare and Ni-doped MoO_3, respectively, compared to the *Mo-terminated (010) facet* (Table S5). The creation of an asymmetric oxygen vacancy is more favorable than a symmetric oxygen vacancy (by ~1.2 eV) and is energetically comparable to the formation of a terminal oxygen vacancy (within ~0.15 eV), which can facilitate easier oxygen desorption, a crucial elementary step in the OER cycle, at the asymmetric oxygen site in MoO_3 (Table S6).[42,64] Additionally, hydrogen atom adsorption at this site is significantly more favorable compared to other oxygen sites (the binding energies of hydrogen adsorbed at asymmetric, terminal, and symmetric oxygen atoms on the MoO_3 (010) surface were determined to be 2.99, 2.77, and 2.11 eV, respectively).[60,64] It is also noteworthy that a previous study ruled out the OER activity of MoO_3 monolayers at the asymmetric oxygen-active sites of the O-terminated (010) facet.[42] Our calculations (Table S7)

Table 1. Standard Gibbs Free Energy Changes Associated with the Elementary Steps Involved in the OER on the Mo-Terminated (010) Facet in Pristine and Ni-Doped MoO_3 Obtained Using PBE + U Calculations[a]

	Elementary Steps	ΔG^0 in Pure MoO_3 (eV)	Elementary Steps	ΔG^0 in Ni-Doped MoO_3 (eV)
1	▲O + H_2O → ▲OOH + $(H^+ + e^-)$	2.36 (η = 1.13 V)	▲O + H_2O → ▲O_2 + H^γ + $(H^+ + e^-)$	−0.90
2	▲OOH → ▲O_2 + $(H^+ + e^-)$	1.21	▲O_2 + H^γ → ▲O_2 + $(H^+ + e^-)$	1.56
3	▲O_2 → ▲ + O_2	0.28	▲O_2 → ▲ + O_2	0.49
4	▲ + H_2O → ▲OH_2	0.17	▲ + H_2O → ▲OH_2	0.04
5	▲OH_2 → ▲OH + $(H^+ + e^-)$	−0.27	▲OH_2 → ▲OH + $(H^+ + e^-)$	1.85
6	▲OH → ▲O + $(H^+ + e^-)$	1.18	▲OH → ▲O + $(H^+ + e^-)$	1.87(η = 0.64 V)

[a]Note that H^γ refers to a proton that gets attached to a nearby oxygen atom in the surface layer of the catalyst, as seen in Figure 2.
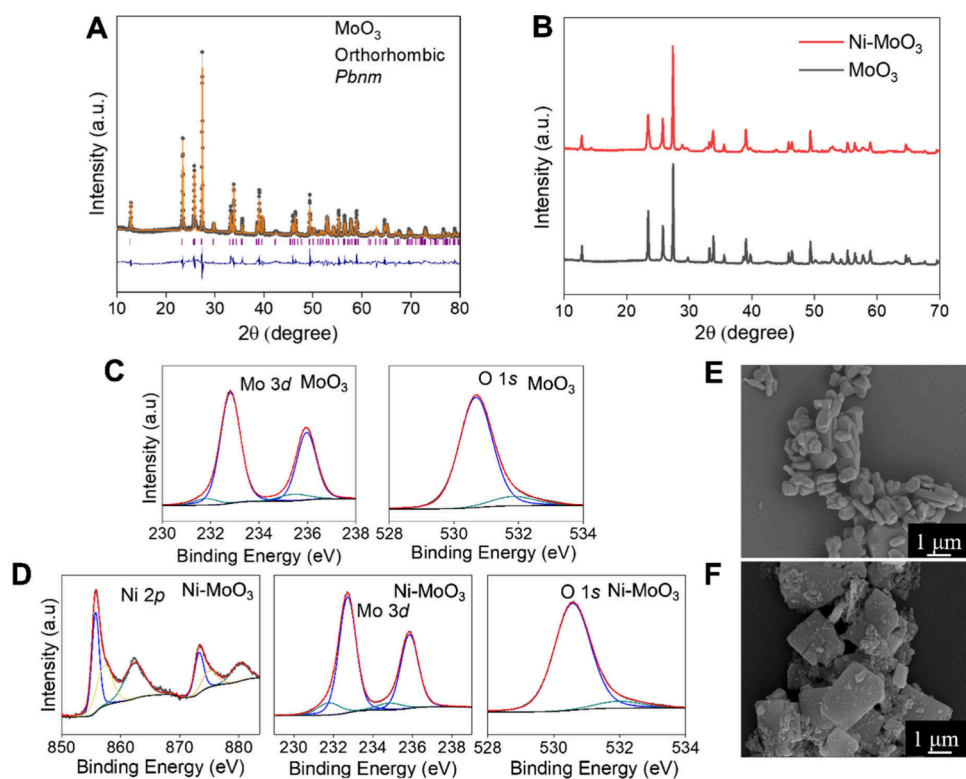

Figure 2. Top views of relaxed structures involved in the associative OER mechanism following three different pathways, determined using the PBE + U method for Ni-doped MoO_3. The standard Gibbs free energy change during each elementary reaction is indicated for all the respective steps. Molybdenum atoms are shown in lilac, oxygen in red, hydrogen in green, and nickel in blue. The overpotential exhibited is 0.64 V.

match the reported results but using the PBE level of theory rather than PBE + U.

We considered the following intermediate moieties involved in the associative OER mechanism: oxo (▲O), hydroperoxo (▲OOH), hydroxo (▲OH), aqua (▲OH_2), and dioxo (▲O_2), where ▲ is the adsite (see Figure 1).[19,26] Figure 1 shows the standard Gibbs free energy profile and the PBE + U-optimized structures of all the adsorbed intermediate configurations involved in the OER cycle on undoped MoO_3. Further, Table 1 reports the standard Gibbs free energy change (ΔG^0) in each elementary step during the OER mechanism. Recall that the evolution of O_2 from two molecules of H_2O needs four proton-coupled electron transfer (PCET) steps.[57] Each elementary reaction step involves distinct intermediates adsorbed on the electrocatalyst. Thermodynamically, the evolution of a single O_2 molecule involves the Gibbs free energy (ΔG) change of 4.92 eV at room temperature. Accordingly, an ideally efficient catalyst requires a ΔG^0 of 1.23 eV for each of the four PCET steps.[65] In this regard, the potential-determining step (PDS) is

the electrochemical elementary step with the highest positive ΔG^0 throughout the OER process, and thermodynamic overpotential corresponds to the difference between ΔG^0 incurred during the PDS and the standard ΔG^0 associated with the OER per electron transferred (1.23 eV).[5] Therefore, the first elementary reaction step in Table 1, i.e., the dissociative adsorption of a water molecule converting the oxo intermediate (▲O) to the hydroperoxo intermediate (▲OOH), is the PDS with the overpotential (η) equal to 1.13 V on pure MoO_3.

In Table 1, we present the thermodynamically most favorable OER mechanism on pure and Ni-doped MoO_3 via four PCET steps and two nonelectrochemical adsorption/desorption steps, with the free energetics determined using the CHE framework (more details in the Methods section). In this framework, the free energy of a proton−electron couple is equal to half that of a hydrogen gas molecule, as the standard hydrogen electrode reaction (H_2 → H^+ + e^-) is assumed to be at equilibrium. Nevertheless, when reported versus the
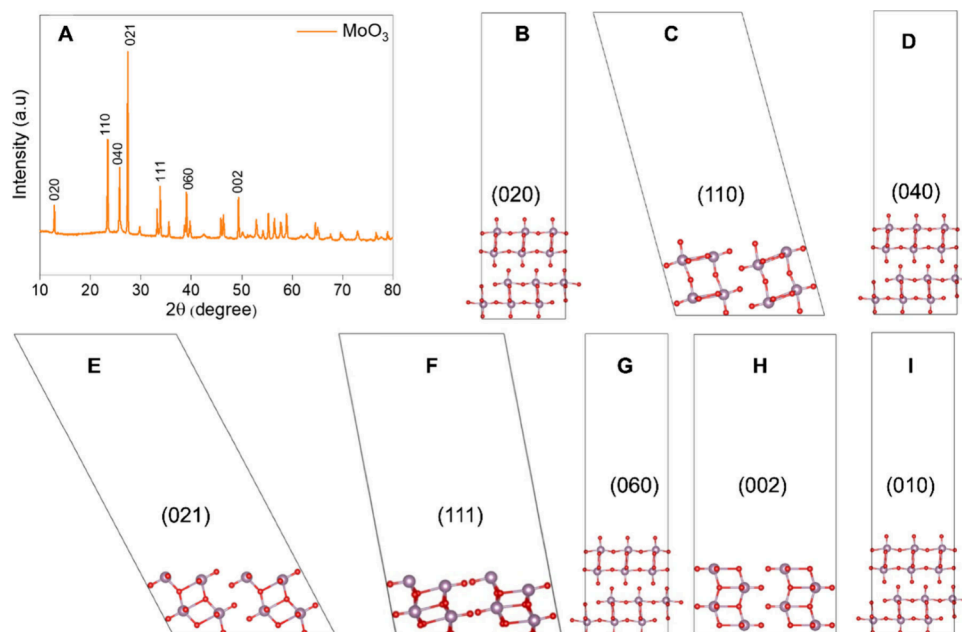
Figure 3. (A) PXRD pattern of MoO_3 with an orthorhombic crystal system and (B) PXRD patterns of bare and Ni-doped MoO_3. High-resolution XPS spectra of (C) Mo 3*d* and O 1*s*, (D) Ni 3*p*, Mo 3*d*, and O 1*s*. FESEM image of (E) MoO_3 showing platelet type morphology and (F) Ni-doped MoO_3 showing agglomerated morphology along with the platelets.

reversible hydrogen electrode (RHE), the reaction Gibbs free energies do not change even when the reactions are written via hydroxide (OH^-) ions rather than protons (H^+) due to the cancellation of Nernstian pH effects. Accordingly, the reported thermodynamics are versus the RHE and are independent of the pH of the medium, being equally applicable at a pH of 14.0, with the reactions written via OH^- ions. Note that for modeling Ni-doped MoO_3, we considered a doping configuration where one out of nine Mo surface ions was replaced with a Ni ion, resulting in approximately 11% Ni doping. Additionally, we explored a higher doping level by replacing two out of nine Mo surface ions with Ni ions, resulting in 22% Ni doping (Figure S2). However, this increased doping concentration led to an undesirable rise in the OER overpotential, from 0.64 to 1.21 V (Table S8). This suggests that excessive Ni incorporation adversely affects the activity of the catalyst. Note that this finding agrees with our experimental results as well, as can be seen later in the text. In Figure 2, we depict the detailed OER mechanism on Ni-doped MoO_3, comparing the typical associative OER pathway with a lattice-oxygen(O^l)-assisted pathway and the hydrogen peroxide (H_2O_2) pathway via the ▲O(OH)H intermediate.

The OER cycle starts with the adsorption of a water molecule on the oxo (▲O) group to produce the hydroperoxo (▲OOH) group, which is the PDS for the mechanism on pure MoO_3. In the next step, the hydroperoxo (▲OOH) group deprotonates to yield dioxo (▲O_2). Subsequently, the dioxo (▲O_2) group is released as an O_2 molecule in a non-electroactive step. The vacancy of the asymmetric oxygen atom is filled by a terminal oxygen (explaining why the vacant site is not visible in Figure 1). Going forward, another non-electroactive step produces the aqua (▲OH_2) group by a

water molecule adsorbing on the vacant (▲) site. In the penultimate step, the aqua (▲OH_2) group deprotonates to the hydroxo (▲OH) group, following which the hydroxo (▲OH) group deprotonates to oxo (▲O). Note that, on Ni-doped MoO_3, the hydroperoxo (▲OOH) breaks into a dioxo and a hydrogen adsorbed to a nearby oxygen, i.e., ▲O_2 + H^γ, which changes the PDS to the step involving the deprotonation of the hydroxo group (▲OH) to form the oxo group (▲O). This is also evident in Table 1, where the overpotential for the OER drops to 0.64 V for the Ni-doped case. We also examined alternative mechanisms involving (i) a lattice oxygen (O^l), called the OO^l mechanism, and (ii) an adsorbed hydrogen peroxide (H_2O_2) molecule, represented as ▲O(OH)H. In the OO^l mechanism, the adsorbed oxygen species (▲O) forms an O−O bond with a neighboring lattice oxygen atom that is nearest to the adsorbed ▲O species.[26] Initially, ▲OH deprotonates and bonds with the nearest lattice oxygen (O^l), forming ▲OO^l. The ▲OO^l species then adsorbs a water molecule, leading to the formation of the ▲OOH species through another deprotonation step (Figure 2). This interaction enables oxygen evolution through a more efficient pathway, reducing the overpotential. These results are tabulated in Tables S9 and S10. As seen therein, the formation of both ▲O(OH)H and ▲OO^l requires a prohibitively high free energy change on pristine MoO_3, ruling out these pathways on the pure material compared to the regular associative OER pathway. On Ni-doped MoO_3, however, both these pathways can occur. Nevertheless, we find that on Ni-doped MoO_3, the formation of ▲O_2 + H^γ is more favorable than the desorption of H_2O_2 (Table S10 and Figure 2), indicating that H_2O_2 will not be formed, but rather the OER cycle will complete.
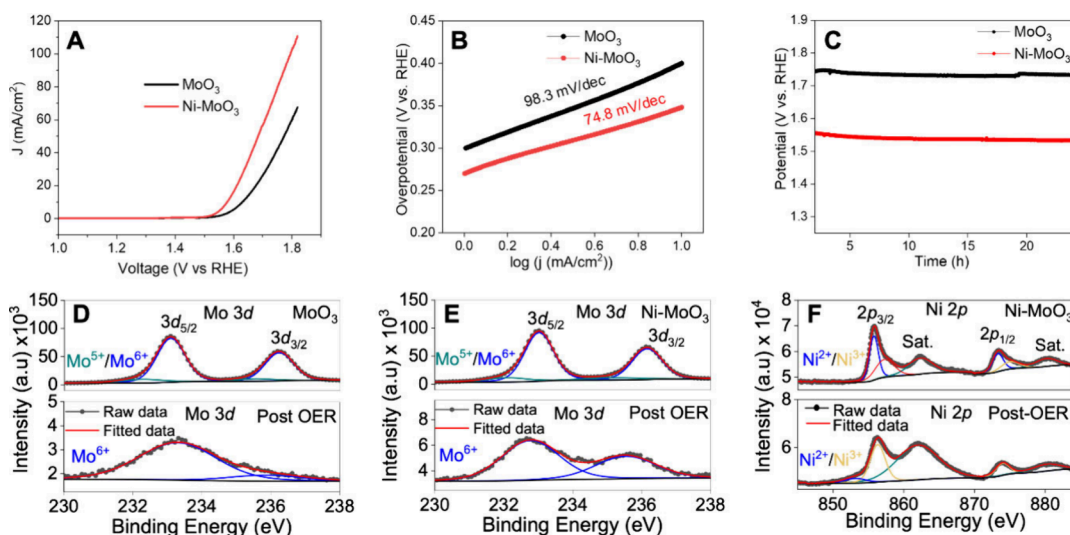
Figure 4. (A) PXRD pattern of MoO_3 with peaks corresponding to various crystallographic facets marked on it. (B−I) Atomic-scale models of the (B) (020), (C) (110), (D) (040), (E) (021), (F) (111), (G) (060), (H) (002), and (I) (010) facets of MoO_3 corresponding to the peaks marked in panel A.

We note that Ni doping significantly alters the electronic structure of MoO_3 by introducing localized states within the band gap and modifying the density of states (DOS) near the Fermi level through the hybridization of Ni d-orbitals with the MoO_3 lattice (Figure S3). These modifications facilitate efficient charge transfer by providing intermediate electronic states, thereby lowering the overpotential required for the OER. Moreover, we found that the Ni−O bond distance in the Ni-doped MoO_3 lattice is slightly larger than the Mo−O bond distance in pure MoO_3, which could improve lattice flexibility (Figure S4). This flexibility could help to accommodate the strain induced during the OER process, possibly preventing lattice degradation and thus improving the catalyst's long-term stability.

Synthesis of the Material and Analysis of Its Surface Morphology via XRD, XPS, and FESEM. Guided by the theoretical prediction of the significant reduction in the OER overpotential of MoO_3 upon doping with nickel, we proceeded to prepare and investigate pure and Ni-doped MoO_3 for their OER activity. Briefly, the synthesis of the catalyst was carried out via a solid-state route using a 10% molar ratio of the nickel precursor. Additionally, we explored higher nickel molar concentrations of 20% and 30% (Figure S5), which led to a deteriorated OER performance. The overpotential values, measured at a current density of 10 mA/cm^2, were determined to be 0.34 V, 0.36 V, and 0.43 V for nickel concentrations of 10%, 20%, and 30%, respectively, indicating 10% to be the optimal Ni doping concentration. Thus, all further analysis was done at a nickel concentration of 10%. The powder X-ray diffraction (PXRD) patterns in Figure 3A and B correspond to MoO_3 and Ni-doped MoO_3. These patterns provide insights into the phase purity and crystal structure of the synthesized material. The crystal structure of MoO_3 is orthorhombic, belonging to the *Pbnm* space group (as indexed in the Inorganic Crystal Structure Database, ICSD #166362). Notably, we found that the powder XRD pattern of Ni-doped MoO_3 shows discernible but not significant alteration

from the XRD pattern of pure MoO_3, indicating the successful incorporation of Ni into the MoO_3 crystal lattice rather than the formation of bulk Ni phases.

Subsequently, XPS was utilized to investigate the oxidation states of the constituent elements in both MoO_3 and Ni-doped MoO_3. Accordingly, high-resolution XPS spectra for Ni, Mo, and O are presented in Figure 3C−D, confirming the presence of these elements on the surface of the synthesized catalysts. The high-resolution XPS (HRXPS) spectra of Mo $3d$ for Ni-doped MoO_3 and pristine MoO_3, as shown in Figure S6, reveal a shift of the Mo $3d$ XPS peaks toward lower binding energy in Ni-doped MoO_3 compared to pure MoO_3. This shift can be ascribed to alterations in the electronic surroundings of the Mo atoms resulting from the incorporation of Ni ions, as seen in the DOS calculations. Moving forward, the surface morphology of the as-synthesized MoO_3 and Ni-doped MoO_3 was investigated using field-emission scanning electron microscopy (FESEM). In Figure 3E, irregularly shaped, smaller platelet-type structures are observed for pure MoO_3. However, after doping with Ni, agglomerated platelets with fine particles adsorbed on top were observed (Figure 3F), an aspect that could be probed via Wulff construction calculations in the future. To better understand the changes in morphology, we also determined the electrochemically active surface area (ECSA) of pure and Ni-doped MoO_3. Cyclic voltammetry (CV) measurements were conducted in the non-Faradaic region at scan rates ranging from 100 mV/s to 500 mV/s, as shown in Figure S7A,B, which were employed to estimate the ECSA. The double-layer capacitance (C_{dl}) was derived by plotting the capacitive current density against the scan rate (Figure S7C). The calculated C_{dl} values were 0.21 mF for Ni-doped MoO_3 and 0.08 mF for pristine MoO_3. Figure S7D presents the ECSA values, with Ni-doped MoO_3 exhibiting a higher ECSA of 5.25 cm^2, which could be attributed to the fine particles adsorbed on top of the agglomerated platelets. BET surface area results corroborated the ECSA measurements. Indeed, Ni-doped MoO_3 exhibited a significantly higher BET

Figure 5. (A) Polarization curves of pure MoO_3 and Ni-doped MoO_3 in alkaline media. (B) Tafel plots for pure and Ni-doped MoO_3 in alkaline media. (C) Chronopotentiometry of pure MoO_3 and Ni-doped MoO_3 at a current density of 10 mA/cm^2. (D−F) XPS spectra of (D) MoO_3 and (E, F) Ni-doped MoO_3 pre (top panel) and post (bottom panel) the OER.

surface area (5.46 m^2/g) compared to undoped MoO_3 (1.13 m^2/g), as shown in Figure S8. The higher surface area leads to the exposure of more sites for interaction with the electrolyte and could contribute to the superior electrocatalytic activity of Ni-doped MoO_3.

In Figure 4A, we show the fitting of the PXRD peaks to crystallographic facets. The prominent facets visible therein are (021), (110), (040), (020), and (060). When the models of these facets were created (Figure 4B−I), we found that the (040), (020), and (060) facets are identical to the MoO_3 basal plane considered in the DFT calculations, thus supporting our model of the catalyst material. Furthermore, DFT calculations revealed that the (021) facet is unstable and undergoes significant reconstruction (Figure S9), and thus, this particular facet was not considered for the OER mechanism calculations.

Electrochemical Performance, Stability, and Comparative Analysis of Bare and Ni-Doped MoO_3. Next, the electrocatalytic performance and stability of pure and Ni-doped MoO_3 were investigated. For carrying out the OER, the active catalyst was drop-cast onto a rotating ring disc electrode (RRDE) used as the working electrode. A bare platinum wire and a Hg/HgO electrode (in 1 M KOH electrolyte, i.e., a pH of 14.0) served as the counter and reference electrodes, respectively. It is noteworthy that the OER catalytic activity of both pure and Ni-doped MoO_3 in acidic media (0.5 M H_2SO_4) was found to be very low. The polarization curves (at a sweep rate of 10 mV/s) at pH 14.0 in Figure 5A were utilized to calculate the overpotential values for pure and Ni-doped MoO_3 at a current density of 10 mA/cm^2 under alkaline conditions. The linear sweep voltammetry (LSV) curves for Ni-doped MoO_3 showed an overpotential value of 0.34 V, lower than that of 0.40 V for pristine MoO_3. Notably, this value is also comparable to RuO_2, a benchmark OER catalyst, which exhibited an overpotential of 0.31 V in alkaline media (Figure S10). In Figure 5B, we carry out Tafel analysis to obtain a Tafel slope of 74.8 mV/dec for Ni-doped MoO_3 under alkaline conditions, which is lower than the value of 98.3 mV/dec for pure MoO_3. We found that the adhesion of the catalyst is weak on the RRDE due to the rotation of the electrode (stable up to about 3 h and 25 cycles of voltammetry), and thus long-time

stability tests up to 24 h were done on a fixed graphite electrode. The stability of the active catalyst was examined by chronopotentiometry after coating the catalyst on a graphite electrode. We found that both pure and Ni-doped MoO_3 remained stable for up to 24 h of constant electrolysis, as seen in Figure 5C. Chronoamperometry results can be seen in Figure S11, revealing a similar conclusion.

Catalytic stability and surface transformations are critical factors in analyzing the long-term durability of the catalyst. After continuous electrolysis for 24 h, although pure MoO_3 maintained its catalytic activity without significant changes, as presented in Figure 5C, we found that quantitative XPS[66] reveals the leaching of Mo from the surface in the KOH electrolyte, as demonstrated by the reduction in the XPS intensity of the Mo peak pre and post-OER (Figure 5D). Note that leaching could lead to a change in morphology or increased surface roughness, which is known to reduce the XPS signal intensity (see Figure S12A for SEM images after the OER and Figure S13 for the XPS spectra).[67] Further, PXRD characterization revealed that the peak intensity drastically reduced for several facets, and the loss of the main peaks confirmed leaching and structural changes after OER electrolysis (Figure S12B). Nevertheless, the fact that pristine MoO_3 provided a stable current under chronopotentiometric conditions indicates that the leaching of MoO_4^{2-} units[68] from the surface continues to expose fresh active catalyst for at least 24 h. For Ni-doped MoO_3, the presence of Ni could promote the formation of $NiOOH/Ni(OH)_2$ on the surface, which could not only enhance activity but also help minimize Mo dissolution by limiting the exposure of MoO_3 moieties. As shown earlier, nickel doping enhances both the electrochemical and bulk surface areas, thereby increasing the exposure of the electrochemical active sites of the material to the electrolyte. Consequently, this reduces the leaching of molybdenum during electrochemical OER. Moving forward, we found that the XPS results for Ni-doped MoO_3 demonstrated a comparatively higher signal strength for Mo after the OER (Figure 5E), thus indicating an increase in the stability of the material. In fact, while the two Mo peaks merge into one (as seen before in a study on nitric acid-treated MoO_3[69]) post the

OER for pure MoO_3, the two peaks of Mo are retained in Ni-doped MoO_3, further indicating the shielding of Mo ions from the alkaline environment. It is noteworthy that XPS only probes the topmost layers (within a few nm) of a material, and thus, the leaching rate is likely slow enough that the catalyst remained stable up to 24 h, as seen from the chronopotentiometric analysis. Finally, the XPS peaks for Ni (Figure 5F) do not change much before and after the OER, implying that the surface regions incorporating it do not leach in alkaline media. Notably, the XPS peak intensities for O in Ni-doped MoO_3 (Figure S13B) also do not change much before and after the OER, as most of the O signal detected likely originates from the adsorbed water molecules rather than the bulk material.[70] In pure MoO_3, however, the O peak broadens (Figure S13A), indicating the formation of surface hydroxyls after the OER[70] (note the favorable OH formation step for pure MoO_3 and more favorable water adsorption on Ni-doped MoO_3, as seen in Table 1). Based on these findings, future work could explore the effect of higher Ni doping concentrations on the stability of the material with respect to Mo leaching.

CONCLUSIONS

We examined the effect of Ni doping on MoO_3 on its OER overpotential and stability, demonstrating the doping of an acidic oxide (MoO_3) by an element that forms a basic oxide (Ni) to be a promising strategy to overcome the activity-stability trade-off for OER catalysts. We first explored the free energetics of the OER on pristine and Ni-doped MoO_3 via DFT calculations at the Hubbard-corrected generalized gradient approximation level of theory for the electronic exchange-correlation interactions. The calculations revealed that Ni doping led to the following changes in the OER mechanism: (i) it changed the PDS from the hydroxylation of the oxo intermediate to form the hydroperoxo intermediate via dissociative water adsorption to the deprotonation of the hydroxo intermediate to form the oxo intermediate; (ii) it led to breakage of the hydroperoxo intermediate to the dioxo plus adsorbed hydrogen intermediate on the doped catalyst; and (iii) it reduced the thermodynamic overpotential by 0.49 V. Apart from the typical associative OER pathway, we showed that lattice-oxygen and hydrogen-peroxide-mediated pathways could also occur on the Ni-doped surface of MoO_3. Moving further, experiments showed that Ni doping of MoO_3 is indeed favorable, leading to overpotentials of 0.34 V and 0.56 V, respectively, at 10 mA/cm^2 and 100 mA/cm^2 OER current density. We also demonstrated that Mo leaches into the KOH solution during the OER via post-mortem XPS, an aspect not examined by previous studies of the OER on pure as well as doped MoO_3. We further showed that Ni doping reduced the extent of Mo leaching, as confirmed via XPS spectra. In the future, one could examine further strategies to stabilize MoO_3 during alkaline water splitting, including the use of higher Ni doping concentrations. Another possibility is to determine the photoelectrochemical water-splitting activity of Ni-doped MoO_3 to harness the power of solar energy. Overall, our work proposes Ni doping as a promising strategy to increase not only the OER activity of MoO_3 but also the stability of the material during alkaline electrochemical water splitting, effectively breaking the usual activity-stability compromise. Moreover, the underlying principle of choosing a dopant advanced in this work is more generally applicable. It can be used to guide the selection of dopants for other electrocatalyst materials as well. Thus, we hope that our work will significantly

impact the development of new materials for electrocatalytic applications.

ASSOCIATED CONTENT

Supporting Information

The Supporting Information is available free of charge at https://pubs.acs.org/doi/10.1021/cbe.4c00160.

> DFT convergence details, OER activity on O-terminated MoO_3 and Ni-doped MoO_3, oxygen vacancy formation energy on the (010) facet, comparison with prior OER modeling results, free energies of the reactions involved in alternative OER pathways, DOS for pure and Ni-doped MoO_3, bond lengths in the MoO_3 lattice, polarization curves of Ni-doped MoO_3 with varying Ni content (10%, 20%, and 30%), XPS spectra for Mo in bare and Ni-doped MoO_3, ECSA measurements, BET adsorption−desorption isotherms of pure and Ni-doped MoO_3, PXRD and FESEM of ex-situ samples, snapshots of the reconstruction of the (021) facet, polarization curves of Ni-doped MoO_3 and RuO_2 in alkaline media, chronoamperometry stability analysis of Ni-MoO_3, XPS spectra of oxygen pre and post the OER on pure and Ni-doped MoO_3, and vibrational modes of the adsorbed atoms on various OER intermediates (PDF)

AUTHOR INFORMATION

Corresponding Author

Ananth Govind Rajan − *Department of Chemical Engineering, Indian Institute of Science, Bengaluru, Karnataka 560012, India;* ⬤ orcid.org/0000-0003-2462-0506; Email: ananthgr@iisc.ac.in

Authors

Ankit Kumar Verma − *Department of Chemical Engineering, Indian Institute of Science, Bengaluru, Karnataka 560012, India; School of Chemistry, Chemical Engineering and Biotechnology, Nanyang Technological University, Singapore 637459, Singapore*

Shahan Atif − *Faraday Materials Laboratory (FaMaL), Materials Research Centre, Indian Institute of Science, Bengaluru, Karnataka 560012, India;* ⬤ orcid.org/0000-0002-0251-2881

Abhisek Padhy − *Faraday Materials Laboratory (FaMaL), Materials Research Centre, Indian Institute of Science, Bengaluru, Karnataka 560012, India*

Tej S. Choksi − *School of Chemistry, Chemical Engineering and Biotechnology, Nanyang Technological University, Singapore 637459, Singapore;* ⬤ orcid.org/0000-0002-9520-019X

Prabeer Barpanda − *Faraday Materials Laboratory (FaMaL), Materials Research Centre, Indian Institute of Science, Bengaluru, Karnataka 560012, India; Helmholtz Institute Ulm (HIU), Electrochemical Energy Storage, Ulm 89081, Germany; Institute of Nanotechnology, Karlsruhe Institute of Technology (KIT), Karlsruhe 76021, Germany;* ⬤ orcid.org/0000-0003-0902-3690

Complete contact information is available at:
https://pubs.acs.org/10.1021/cbe.4c00160

Notes

The authors declare no competing financial interest.

■ REFERENCES

(1) Das, D.; Veziroglu, T. N. Hydrogen Production by Biological Processes: A Survey of Literature. *Int. J. Hydrogen Energy* **2001**, *26* (1), 13−28.

(2) Esposito, D.; Antonietti, M. Redefining Biorefinery: The Search for Unconventional Building Blocks for Materials. *Chem. Soc. Rev.* **2015**, *44* (16), 5821−5835.

(3) Wexler, R. B.; Stechel, E. B.; Carter, E. A. Materials Design Directions for Solar Thermochemical Water Splitting. *Solar Fuels* **2023**, 1−63.

(4) Walter, M. G.; Warren, E. L.; McKone, J. R.; Boettcher, S. W.; Mi, Q.; Santori, E. A.; Lewis, N. S. Solar Water Splitting Cells. *Chem. Rev.* **2010**, *110* (11), 6446−6473.

(5) Govind Rajan, A.; Martirez, J. M. P.; Carter, E. A. Why Do We Use the Materials and Operating Conditions We Use for Heterogeneous (Photo)Electrochemical Water Splitting? *ACS Catal.* **2020**, *10* (19), 11177−11234.

(6) Song, J.; Wei, C.; Huang, Z.-F.; Liu, C.; Zeng, L.; Wang, X.; Xu, Z. J. A Review on Fundamentals for Designing Oxygen Evolution Electrocatalysts. *Chem. Soc. Rev.* **2020**, *49* (7), 2196−2214.

(7) Ledendecker, M.; Clavel, G.; Antonietti, M.; Shalom, M. Highly Porous Materials as Tunable Electrocatalysts for the Hydrogen and Oxygen Evolution Reaction. *Adv. Funct. Mater.* **2015**, *25* (3), 393−399.

(8) Govind Rajan, A.; Carter, E. A. Microkinetic Model for pH- and Potential-Dependent Oxygen Evolution during Water Splitting on Fe-Doped β-NiOOH. *Energy Environ. Sci.* **2020**, *13* (12), 4962−4976.

(9) You, B.; Sun, Y. Innovative Strategies for Electrocatalytic Water Splitting. *Acc. Chem. Res.* **2018**, *51* (7), 1571−1580.

(10) Govind Rajan, A.; Martirez, J. M. P.; Carter, E. A. Coupled Effects of Temperature, Pressure, and pH on Water Oxidation Thermodynamics and Kinetics. *ACS Catal.* **2021**, *11* (18), 11305−11319.

(11) Zhu, Y. P.; Guo, C.; Zheng, Y.; Qiao, S.-Z. Surface and Interface Engineering of Noble-Metal-Free Electrocatalysts for Efficient Energy Conversion Processes. *Acc. Chem. Res.* **2017**, *50* (4), 915−923.

(12) Meyer, J.; Hamwi, S.; Kröger, M.; Kowalsky, W.; Riedl, T.; Kahn, A. Transition Metal Oxides for Organic Electronics: Energetics, Device Physics and Applications. *Adv. Mater.* **2012**, *24* (40), 5408−5427.

(13) Wang, J.; Xu, L.; Lu, Y.; Sheng, K.; Liu, W.; Chen, C.; Li, Y.; Dong, B.; Song, H. Engineered IrO_2@NiO Core-Shell Nanowires for Sensitive Non-Enzymatic Detection of Trace Glucose in Saliva. *Anal. Chem.* **2016**, *88* (24), 12346−12353.

(14) Louie, M. W.; Bell, A. T. An Investigation of Thin-Film Ni-Fe Oxide Catalysts for the Electrochemical Evolution of Oxygen. *J. Am. Chem. Soc.* **2013**, *135* (33), 12329−12337.

(15) Yao, L.; Zhang, H.; Humayun, M.; Fu, Y.; Xu, X.; Feng, C.; Wang, C. Constructing Nanoporous Crystalline/Amorphous $NiFe_2O_4$/NiO Electrocatalyst for High Efficiency OER/UOR. *J. Alloys Compd.* **2023**, *936*, 168206.

(16) Wang, Q.; Huang, X.; Zhao, Z. L.; Wang, M.; Xiang, B.; Li, J.; Feng, Z.; Xu, H.; Gu, M. Ultrahigh-Loading of Ir Single Atoms on NiO Matrix to Dramatically Enhance Oxygen Evolution Reaction. *J. Am. Chem. Soc.* **2020**, *142* (16), 7425−7433.

(17) Liu, J.; Xiao, J.; Wang, Z.; Yuan, H.; Lu, Z.; Luo, B.; Tian, E.; Waterhouse, G. I. N. Structural and Electronic Engineering of Ir-Doped Ni-(Oxy)Hydroxide Nanosheets for Enhanced Oxygen Evolution Activity. *ACS Catal.* **2021**, *11* (9), 5386−5395.

(18) Zhang, B.; Wang, L.; Cao, Z.; Kozlov, S. M.; García de Arquer, F. P.; Dinh, C. T.; Li, J.; Wang, Z.; Zheng, X.; Zhang, L.; Wen, Y.; Voznyy, O.; Comin, R.; De Luna, P.; Regier, T.; Bi, W.; Alp, E. E.; Pao, C.-W.; Zheng, L.; Hu, Y.; Ji, Y.; Li, Y.; Zhang, Y.; Cavallo, L.; Peng, H.; Sargent, E. H. High-Valence Metals Improve Oxygen Evolution Reaction Performance by Modulating $3d$ Metal Oxidation Cycle Energetics. *Nat. Catal.* **2020**, *3* (12), 985−992.

(19) Govind Rajan, A.; Martirez, J. M. P.; Carter, E. A. Facet-Independent Oxygen Evolution Activity of Pure β-NiOOH: Different Chemistries Leading to Similar Overpotentials. *J. Am. Chem. Soc.* **2020**, *142* (7), 3600−3612.

(20) Escalera-López, D.; Czioska, S.; Geppert, J.; Boubnov, A.; Röse, P.; Saraçi, E.; Krewer, U.; Grunwaldt, J.-D.; Cherevko, S. Phase- and Surface Composition-Dependent Electrochemical Stability of Ir-Ru Nanoparticles during Oxygen Evolution Reaction. *ACS Catal.* **2021**, *11* (15), 9300−9316.

(21) Huang, J.; Sheng, H.; Ross, R. D.; Han, J.; Wang, X.; Song, B.; Jin, S. Modifying Redox Properties and Local Bonding of Co_3O_4 by CeO_2 Enhances Oxygen Evolution Catalysis in Acid. *Nat. Commun.* **2021**, *12* (1), 3036.

(22) Zakharova, G. S.; Fattakhova, Z. A.; Zhu, Q.; Enyashin, A. N. Ion Sensor Activity of α-MoO_3 Prepared Using Microwave-Assisted Hydrothermal Synthesis. *J. Electroanal. Chem.* **2019**, *840*, 187−192.

(23) Fu, X.; Yang, P.; Xiao, X.; Zhou, D.; Huang, R.; Zhang, X.; Cao, F.; Xiong, J.; Hu, Y.; Tu, Y.; Zou, Y.; Wang, Z.; Gu, H. Ultra-Fast and Highly Selective Room-Temperature Formaldehyde Gas Sensing of Pt-Decorated MoO_3 Nanobelts. *J. Alloys Compd.* **2019**, *797*, 666−675.

(24) Camacho-Forero, L. E.; Godínez-Salomón, F.; Ramos-Sánchez, G.; Rhodes, C. P.; Balbuena, P. B. Theoretical and Experimental Study of the Effects of Cobalt and Nickel Doping within IrO_2 on the Acidic Oxygen Evolution Reaction. *J. Catal.* **2022**, *408*, 64−80.

(25) Li, N.; Bediako, D. K.; Hadt, R. G.; Hayes, D.; Kempa, T. J.; von Cube, F.; Bell, D. C.; Chen, L. X.; Nocera, D. G. Influence of Iron Doping on Tetravalent Nickel Content in Catalytic Oxygen Evolving Films. *Proc. Natl. Acad. Sci. U. S. A.* **2017**, *114* (7), 1486−1491.

(26) Govind Rajan, A.; Martirez, J. M. P.; Carter, E. A. Strongly Facet-Dependent Activity of Iron-Doped β-Nickel Oxyhydroxide for the Oxygen Evolution Reaction. *Phys. Chem. Chem. Phys.* **2024**, *26* (20), 14721−14733.

(27) Guha, P.; Mohanty, B.; Thapa, R.; Kadam, R. M.; Satyam, P. V.; Jena, B. K. Defect-Engineered MoO_2 Nanostructures as an Efficient Electrocatalyst for Oxygen Evolution Reaction. *ACS Appl. Energy Mater.* **2020**, *3* (6), 5208−5218.

(28) Verma, A. K.; Verma, A. M.; Govind Rajan, A. Theoretical Understanding of Electrochemical Phenomena in 2D Electrode Materials. *Curr. Opin. Electrochem.* **2022**, *36*, 101116.

(29) Zhang, X.; Feng, C.; Dong, B.; Liu, C.; Chai, Y. High-Voltage-Enabled Stable Cobalt Species Deposition on MnO_2 for Water Oxidation in Acid. *Adv. Mater.* **2023**, *35* (13), 2207066.

(30) Wang, S.; Liu, L.; Xin, H.; Ling, C. Toward a Stable and Active Catalyst for Proton-Exchange Membrane Water Electrolysis. *Chem. Catal.* **2024**, *4* (1), 100869.

(31) Etzi Coller Pascuzzi, M.; Hofmann, J. P.; Hensen, E. J. M. Promoting Oxygen Evolution of IrO_2 in Acid Electrolyte by Mn. *Electrochim. Acta* **2021**, *366*, 137448.

(32) Keerthana, S. P.; Rani, B. J.; Ravi, G.; Yuvakkumar, R.; Hong, S. I.; Velauthapillai, D.; Saravanakumar, B.; Thambidurai, M.; Dang, C. Ni Doped Bi_2WO_6 for Electrochemical OER Activity. *Int. J. Hydrogen Energy* **2020**, *45* (38), 18859−18866.

(33) Kundu, J.; Khilari, S.; Bhunia, K.; Pradhan, D. Ni-Doped CuS as an Efficient Electrocatalyst for the Oxygen Evolution Reaction. *Catal. Sci. Technol.* **2019**, *9* (2), 406−417.

(34) Peng, Y.; Hajiyani, H.; Pentcheva, R. Influence of Fe and Ni Doping on the OER Performance at the $Co_3O_4(001)$ Surface: Insights from DFT+U. *ACS Catal.* **2021**, *11* (9), 5601−5613.

(35) Yan, Y.; Xia, B.; Xu, Z.; Wang, X. Recent Development of Molybdenum Sulfides as Advanced Electrocatalysts for Hydrogen Evolution Reaction. *ACS Catal.* **2014**, *4* (6), 1693−1705.

(36) Peng, Z.; Wang, K.; Xu, W.; Wang, B.; Mao, B.; Han, Y.; Tsung, C.-K.; Yang, B.; Liu, Z.; Li, Y. Strong Interface Enhanced Hydrogen Evolution over Molybdenum-Based Catalysts. *ACS Appl. Energy Mater.* **2020**, *3* (6), 5219−5228.

(37) Zhao, J.; Ren, X.; Ma, H.; Sun, X.; Zhang, Y.; Yan, T.; Wei, Q.; Wu, D. Synthesis of Self-Supported Amorphous $CoMoO_4$ Nanowire Array for Highly Efficient Hydrogen Evolution Reaction. *ACS Sustain. Chem. Eng.* **2017**, *5* (11), 10093−10098.

(38) Jansi Rani, B.; Ravi, G.; Yuvakkumar, R.; Ameen, F.; AlNadhari, S.; Hong, S. I. Fabrication and Electrochemical OER Activity of Ag Doped MoO_3 Nanorods. *Mater. Sci. Semicond. Process.* **2020**, *107*, 104818.

(39) Tariq, M.; Zaman, W. Q.; Sun, W.; Zhou, Z.; Wu, Y.; Cao, L.; Yang, J. Unraveling the Beneficial Electrochemistry of IrO_2/MoO_3 Hybrid as a Highly Stable and Efficient Oxygen Evolution Reaction Catalyst. *ACS Sustain. Chem. Eng.* **2018**, *6* (4), 4854−4862.

(40) Li, X.; Wang, Y.; Wang, J.; Da, Y.; Zhang, J.; Li, L.; Zhong, C.; Deng, Y.; Han, X.; Hu, W. Sequential Electrodeposition of Bifunctional Catalytically Active Structures in $MoO_3/Ni-NiO$ Composite Electrocatalysts for Selective Hydrogen and Oxygen Evolution. *Adv. Mater.* **2020**, *32* (39), 2003414.

(41) Kim, K.-H.; Hong, D.; Kim, M. G.; Choi, W.; Min, T.; Kim, Y.-M.; Choi, Y.-H. Improving Electrocatalytic Activity of MoO_3 for the Oxygen Evolution Reaction by Incorporation of Li Ions. *ACS Mater. Lett.* **2023**, *5* (4), 1196−1201.

(42) Wang, S.; Ren, Z.; Yu, S.; Huang, B.; Dai, Y.; Wei, W. Structure Engineering of MoO_3 Breaks the Scaling Relationship and Achieves High Electrocatalytic Oxygen Evolution Activity in Acidic Conditions. *J. Mater. Chem. A* **2023**, *11* (27), 14952−14958.

(43) Liu, Y.; Liu, P.; Men, Y.-L.; Li, Y.; Peng, C.; Xi, S.; Pan, Y.-X. Incorporating MoO_3 Patches into a Ni Oxyhydroxide Nanosheet Boosts the Electrocatalytic Oxygen Evolution Reaction. *ACS Appl. Mater. Interfaces* **2021**, *13* (22), 26064−26073.

(44) Karmakar, A.; Karthick, K.; Sankar, S. S.; Kumaravel, S.; Ragunath, M.; Kundu, S. Oxygen Vacancy Enriched $NiMoO_4$ Nanorods *via* Microwave Heating: A Promising Highly Stable Electrocatalyst for Total Water Splitting. *J. Mater. Chem. A* **2021**, *9* (19), 11691−11704.

(45) Armstrong, R. D.; Bell, M. F.; Metcalfe, A. A. The Anodic Dissolution of Molybdenum in Alkaline Solutions — Electrochemical

(46) Jin, S. Are Metal Chalcogenides, Nitrides, and Phosphides Oxygen Evolution Catalysts or Bifunctional Catalysts? *ACS Energy Lett.* **2017**, *2* (8), 1937−1938.

(47) Kresse, G.; Furthmüller, J. Efficiency of Ab-Initio Total Energy Calculations for Metals and Semiconductors Using a Plane-Wave Basis Set. *Comput. Mater. Sci.* **1996**, *6* (1), 15−50.

(48) Kresse, G.; Furthmüller, J.; Hafner, J. Theory of the Crystal Structures of Selenium and Tellurium: The Effect of Generalized-Gradient Corrections to the Local-Density Approximation. *Phys. Rev. B* **1994**, *50* (18), 13181−13185.

(49) Kresse, G.; Joubert, D. From Ultrasoft Pseudopotentials to the Projector Augmented-Wave Method. *Phys. Rev. B* **1999**, *59* (3), 1758−1775.

(50) Blöchl, P. E. Projector Augmented-Wave Method. *Phys. Rev. b* **1994**, *50* (24), 17953−17979.

(51) Perdew, J. P.; Burke, K.; Ernzerhof, M. Generalized Gradient Approximation Made Simple. *Phys. Rev. Lett.* **1996**, *77* (18), 3865−3868.

(52) Dudarev, S. L.; Botton, G. A.; Savrasov, S. Y.; Humphreys, C. J.; Sutton, A. P. Electron-Energy-Loss Spectra and the Structural Stability of Nickel Oxide: An LSDA+U Study. *Phys. Rev. B* **1998**, *57* (3), 1505−1509.

(53) Coquet, R.; Willock, D. J. The (010) Surface of α-MoO_3, a DFT + U Study. *Phys. Chem. Chem. Phys.* **2005**, *7* (22), 3819−3828.

(54) Li, Y.-F.; Selloni, A. Mechanism and Activity of Water Oxidation on Selected Surfaces of Pure and Fe-Doped NiO_X. *ACS Catal.* **2014**, *4* (4), 1148−1153.

(55) Monkhorst, H. J.; Pack, J. D. Special Points for Brillouin-Zone Integrations. *Phys. Rev. B* **1976**, *13* (12), 5188−5192.

(56) Nørskov, J. K.; Rossmeisl, J.; Logadottir, A.; Lindqvist, L.; Kitchin, J. R.; Bligaard, T.; Jónsson, H. Origin of the Overpotential for Oxygen Reduction at a Fuel-Cell Cathode. *J. Phys. Chem. B* **2004**, *108* (46), 17886−17892.

(57) Rossmeisl, J.; Logadottir, A.; Nørskov, J. K. Electrolysis of Water on (Oxidized) Metal Surfaces. *Chem. Phys.* **2005**, *319* (1), 178−184.

(58) *NIST-JANAF Thermochemical Tables.* https://janaf.nist.gov/.

(59) Henkelman, G.; Uberuaga, B. P.; Jónsson, H. A Climbing Image Nudged Elastic Band Method for Finding Saddle Points and Minimum Energy Paths. *J. Chem. Phys.* **2000**, *113* (22), 9901−9904.

(60) Lei, Y.-H.; Chen, Z.-X. DFT+U Study of Properties of MoO_3 and Hydrogen Adsorption on MoO_3 (010). *J. Phys. Chem. C* **2012**, *116* (49), 25757−25764.

(61) Kihlborg, L. Least Squares Refinement of Crystal Structure of Molybdenum Trioxide. *Ark. Kemi* **1963**, *21*, 357−364.

(62) Chippindale, A. M.; Cheetham, A. K. Chapter 3 - The Oxide Chemistry of Molybdenum. In *Molybdenum*; Braithwaite, E. R., Haber, J., Eds.; Elsevier, 1994; Vol. *19*, pp 146−184.

(63) Choksi, T.; Greeley, J. Partial Oxidation of Methanol on MoO_3 (010): A DFT and Microkinetic Study. *ACS Catal.* **2016**, *6* (11), 7260−7277.

(64) Chen, L.; Pez, G.; Cooper, A. C.; Cheng, H. A Mechanistic Study of Hydrogen Spillover in MoO_3 and Carbon-Based Graphitic Materials. *J. Phys.: Condens. Matter* **2008**, *20* (6), 064223.

(65) Govind Rajan, A.; Carter, E. A. Discovering Competing Electrocatalytic Mechanisms and Their Overpotentials: Automated Enumeration of Oxygen Evolution Pathways. *J. Phys. Chem. C* **2020**, *124* (45), 24883−24898.

(66) Sprenger, D.; Bach, H.; Meisel, W.; Gütlich, P. Quantitative XPS Analysis of Leached Layers on Optical Glasses. *Surf. Interface Anal.* **1993**, *20* (9), 796−802.

(67) Fulghum, J. E.; Linton, R. W. Quantitation of Coverages on Rough Surfaces by XPS: An Overview. *Surf. Interface Anal.* **1988**, *13* (4), 186−192.

(68) Hoh, K. The Anodic Dissolution of Molybdenum in Acidic Nitrate Solutions, University of Missouri—Rolla, 1970. https://scholarsmine.mst.edu/masters_theses/7036/.

Measurements. *J. Electroanal. Chem. Interfacial Electrochem.* **1977**, *84* (1), 61−72.

(69) Huang, S.; Liu, H.; Zhang, L.; Liu, S.; Xin, W.; Li, X.; Xie, S.; Xu, L. Effects of Acid Leaching Post-Treatment on the Catalytic Performance of MoO$_3$/Mordenite-Alumina Catalysts for 1-Butene Metathesis Reaction. *Appl. Catal. A Gen.* **2011**, *404* (1), 113−119.

(70) Idriss, H. On the Wrong Assignment of the XPS O1s Signal at 531−532 eV Attributed to Oxygen Vacancies in Photo- and Electro-Catalysts for Water Splitting and Other Materials Applications. *Surf. Sci.* **2021**, *712*, 121894.